Nonintrusive Motor Current Signature Analysis

Thomas C. Krause, *Graduate Student Member, IEEE*, Łukasz Huchel, Daisy H. Green, *Member, IEEE*, Kahyun Lee, and Steven B. Leeb, *Fellow, IEEE*

***Abstract*— Motor current signature analysis (MCSA) techniques measure slip-related current signals in the supply lines of a squirrel-cage induction machine (SCIM) for slip estimation, fault detection, and motor diagnostics. In a traditional setup for MCSA, current sensors directly measure the machine currents and are usually installed physically close to the machine of interest, e.g., current transducers clamped about the machine stator leads. For grid-connected SCIMs, the slip-related current signals propagate through the power system. Thus, a single aggregate power monitor can potentially perform MCSA for a collection of SCIMs powered by a common electrical service, referred to in this article as nonintrusive MCSA. Current division and system impedances (source impedance, load impedances, and machine parameters) determine the applicability of nonintrusive MCSA. This article demonstrates measurement hardware, modeling, and experimental results for nonintrusive MCSA. Analysis and results investigate the current-source model of a grid-connected SCIM and its interaction with the system impedances. Applied to a distribution system with multiple machines, the techniques inform when nonintrusive MCSA is possible for collections of SCIMs and equivalent to traditional MCSA.**

***Index Terms*— Induction machines, power monitoring, slot harmonics.**

I. Introduction

GRID-CONNECTED squirrel cage induction machines (SCIMs) are workhorse components of industry that draw significant current at the utility frequency to do work. They also exhibit slip-related current signals in their supply lines associated with nonfundamental frequency variations in the motor air-gap flux from winding configuration, rotor bar structure, and variable air-gap reluctance. Motor current signature analysis (MCSA) uses motor-current measurements to diagnose motor and mechanical-system faults such as broken rotor bars, roller-bearing faults, and abnormal air-gap eccentricity [1], [2], [3], [4], [5], [6], [7], [8], [9]. Sidebands around the utility-frequency current component are often indicative of rotor-bar faults. Higher-frequency current signals, referred to as rotor slot harmonics, offer insights into rotor eccentricity and rotor-bar faults [10], [11]. The principle slot harmonic (PSH) is commonly used for slip estimation [12], [13], [14], [15]. Fig. 1 shows an example of the signals commonly used for MCSA, where the singled-sided discrete Fourier transform (DFT) magnitude spectrum of the phase current of a 1.5 hp SCIM [16] connected to a 60 Hz grid and operating at rated slip is plotted. A notch filter removed the utility-frequency component before sampling. Numerous frequency components are present, including utility-frequency harmonics, sidebands around 60 Hz, and slot harmonics. The most prominent signal is the PSH located at 988 Hz.

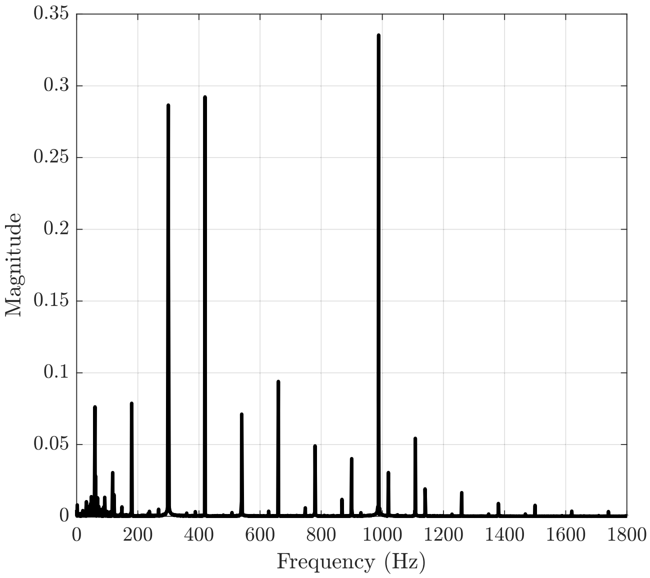

Fig. 1. Singled-sided DFT magnitude spectrum of the phase current of an SCIM.

Traditional MCSA uses current measurement devices around the motor power cables, usually installed physically close to the motor. Aggregate power monitors, also known as nonintrusive load monitors (NILMs), use current measurement devices to monitor an aggregate current feeding many loads. Nonintrusive monitoring is therefore remote from any particular device. Nonintrusive monitoring can differentiate individual load signatures from the aggregate power stream [17] by analyzing changes in current consumption at the utility frequency, e.g., 50 or 60 Hz. This article exploits tailored instrumentation that rejects the utility-frequency current component, enabling a NILM to measure relatively tiny, nonutility-frequency currents such as rotor slot harmonics from grid-connected SCIMs

---

Manuscript received 17 August 2022; revised 1 November 2022; accepted 5 December 2022. Date of publication 2 January 2023; date of current version 11 January 2023. This work was supported in part by the Office of Naval Research Structural Acoustics Program and in part by the Grainger Foundation. The Associate Editor coordinating the review process was Dr. Ferdinanda Ponci. *(Corresponding author: Thomas C. Krause.)*

Thomas C. Krause and Steven B. Leeb are with the Department of Electrical Engineering and Computer Science, Massachusetts Institute of Technology, Cambridge, MA 02139 USA (e-mail: tkrause@mit.edu; sbleeb@mit.edu).

Łukasz Huchel is with Enphase Energy, Austin, TX 78758 USA.

Daisy H. Green is with the Department of Architecture, Massachusetts Institute of Technology, Cambridge, MA 02139 USA.

Kahyun Lee is with the Department of Electronic and Electrical Engineering, Ewha Womans University, Seoul 03760 South Korea.

Digital Object Identifier 10.1109/TIM.2022.3232645

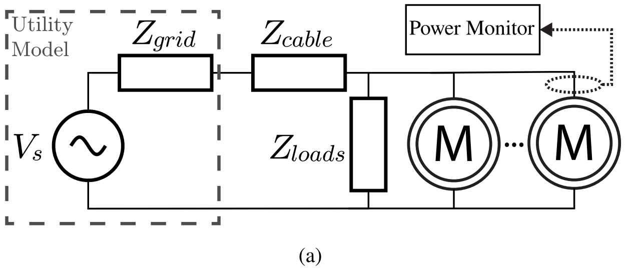

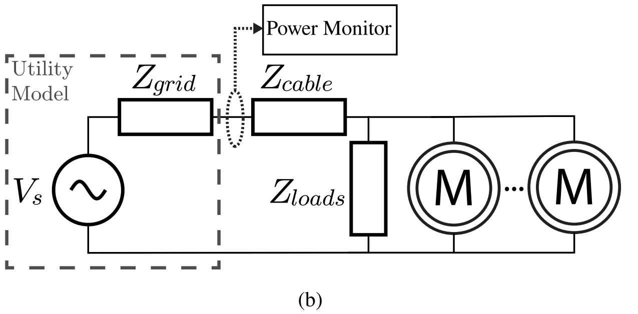

Fig. 2. Comparison between MCSA methods (a) traditional MCSA and (b) nonintrusive MCSA. The power monitor box and associated current-sensing loop (dashed line) represent the installation point of current-measurement devices.

with adequate dynamic range [14], [18]. This instrumentation enables the measurement of subtle current signals and the application of MCSA techniques for grid-connected SCIMs by a NILM referred to in this article as nonintrusive MCSA.

Fig. 2 illustrates the difference in current measurement locations for a traditional MCSA setup and a nonintrusive MCSA setup. These diagrams describe single-phase systems or polyphase systems (in a per-phase impedance diagram sense). An ideal voltage source V_s and equivalent impedance Z_{grid} (surrounded by a box with dashed lines) form the utility model and encompass the parameters of generators, transformers, transmission lines, and any connected loads upstream from the nonintrusive monitoring point. Z_{cable} describes the impedance of any cabling between the nonintrusive monitoring point and a load connection point. Aggregate power monitors are usually installed at the service entry or at a subpanel to monitor a specific set of loads. Z_{cable} is often ignored or incorporated into Z_{grid}, however, in Fig. 2(a) it clarifies the physical distance between the loads and the power monitor. The impedance Z_{loads} is a lumped model for all other loads and their cabling as seen from a load connection point. Of course, viewed from a specific load connection point, there is also a cable impedance (not pictured) for any other load not included in Z_{loads}, for example, the motors on the right side of the diagrams. The current-measurement location (power monitor location) distinguishes Fig. 2(a) from Fig. 2(b). In Fig. 2(a), current measurement devices are associated with the circuit branch of an individual machine. In Fig. 2(b), current measurement devices are associated with the distribution branch feeding many loads.

When possible, nonintrusive MCSA enables a single monitor to measure important health- and operating-condition-related current signals for a group of SCIMs [15]. Nonintrusive MCSA is an especially useful alternative when many sensors for individual motors are too expensive, intrusive, or dangerous to install. Other articles consider nonintrusive MCSA, however, the existing literature assumes the power-system impedances permit an aggregate power monitor to measure all slip-related current signals from a grid-connected SCIM [14], [15], [18], [19]. Although valid for their specific situations, this assumption may not always hold. This article provides a deeper study of nonintrusive MCSA than available in the present literature.

Among many, there are two prevailing challenges with nonintrusive MCSA: disaggregation of specific current signals from the aggregate measurements and current division across the branches of the distribution network. Other articles consider the disaggregation problem. O'Connell et al. [15] demonstrate nonintrusive MCSA for ventilation system diagnostics and identity, disaggregate, and track current signals from multiple grid-connected machines in a marine-microgrid environment. In contrast with previous work such as [14], [15], [19], and [20], the analysis in this article addresses the current division aspects of nonintrusive MCSA. The contributions of this article include answers to questions that govern when and how nonintrusive MCSA will be successful, including: What is an appropriate model for grid-connected SCIM current signals? How do grid-connected SCIM current signals interact with power system impedances? Are all higher-frequency current signals from a remote grid-connected SCIM present in the NILM current measurements? If present, are they distorted such that their diagnostic utility is lost or modified?

This article demonstrates a modeling technique for determining when nonintrusive monitoring of higher-frequency current signals is possible on a grid or grid section. Analysis and experiments examine the PSHs for grid-connected SCIMs. The proposed modeling techniques are verified experimentally and use cases are discussed. The analysis presented in this article clarifies under what conditions the current signals measured by a NILM are equivalent to the current signals measured by traditional MCSA. The outline of this work is the following. Section II reviews slip-related current signals from SCIMs. Section III presents custom power monitor instrumentation. Section IV experimentally compares traditional MCSA and nonintrusive MCSA. Section V discusses nonlinear loads and SCIM current-source models. Section VI introduces modeling techniques and examines the effect of connected loads on the signals measured by a NILM. Section VII presents experimental results. Section VIII discusses some of the practical challenges of nonintrusive MCSA.

II. SQUIRREL-CAGE INDUCTION MOTORS AND CURRENT SIGNALS

Practical SCIMs exhibit nonsinusoidal winding distributions, nonuniform air gap, and are driven with voltages with significant nonfundamental frequency content [21], [22]. These practical factors give rise to phenomena such as the higher-frequency slip-related current signals of SCIMs. This section reviews higher-frequency slip-related current signals in the

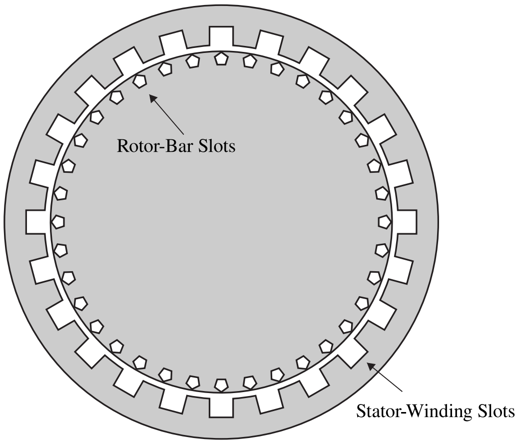

Fig. 3. Stator and rotor structure of a SCIM.

supply lines of SCIMs, specifically, the rotor slot harmonics. For MCSA, spatial harmonics in the air-gap flux caused by the squirrel-cage rotor construction are of high importance [23].

Fig. 3 shows a conceptual diagram of the stator and rotor of a SCIM. Coils of conductive wire in the stator slots form the stator windings. In well-designed machines, the stator-winding configuration typically creates an air-gap magnetomotive force (MMF) that is well-approximated by a sinusoidal function [22]. Aluminum or copper rotor bars occupy the uniformly-distributed rotor-bar slots. Ring-shaped end caps short-circuit the rotor bars and form the squirrel-cage rotor. The structure of the squirrel-cage rotor adds significant harmonic content to the rotor air-gap MMF. The resultant harmonic flux induces current signals in the stator windings of the motor called rotor slot harmonics. For most motors, the rotor MMF is the dominant contributing factor of rotor slot harmonics [23]. Variable air-gap reluctance due to slotting or eccentricity also contributes to nonfundamental air-gap flux and rotor slot harmonics. MCSA techniques commonly use eccentricity or broken rotor bar-caused changes in rotor slot harmonics to diagnose faults [10], [11].

The frequencies of the rotor slot harmonics are

$$f = f_e\left[(kR + n_d)\frac{1-s}{p/2} + \upsilon\right] \tag{1}$$

where f_e is the frequency of the electrical supply, k is the order of rotor slot harmonics, R is the number of rotor bars or slots, p is the number of poles, $n_d = 0, \pm 1, \ldots$ is the order of rotor eccentricity or decentering, s is the slip, and $\upsilon = \pm 1, \pm 3, \ldots$ is the order of the stator-MMF harmonics [18]. Equation (1) includes current signals due to higher-order stator-MMF harmonics and eccentricity. The PSH only depends on the fundamental stator MMF component and the number of rotor slots, i.e., $n_d = 0$, $\upsilon = 1$, and $k = 1$. The frequency of the PSH is

$$f_{\text{psh}} = f_e\left[\frac{R(1-s)}{p/2} + 1\right]. \tag{2}$$

Detailed explanations and derivations of (1) are given by multiple authors, for example [21], [24], and [25]. In this article, analysis and experiments focus on the PSH due to its industrial relevance and experimental considerations discussed in Section VII. However, the techniques presented in Section VI apply to any slot harmonic described by (1) or, more generally, any nonfundamental current signal produced by a load.

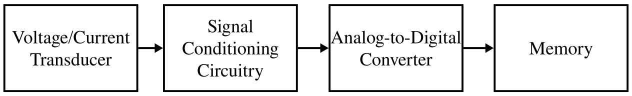

Fig. 4. General power monitor signal path.

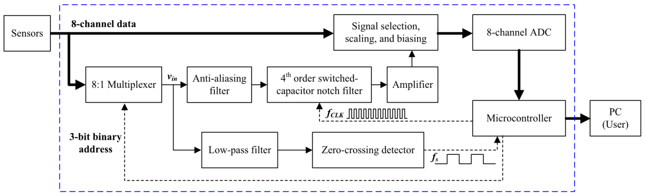

Fig. 5. Custom power monitor block diagram [18].

III. Power Monitor Instrumentation

Section II reviewed slip-related current signals generated by SCIMs. This section reviews typical power-monitor instrumentation and presents specific circuitry that enables the measurement of small nonfundamental frequency signals, such as rotor slot harmonics.

Fig. 4 shows a block diagram of a power monitor signal-acquisition path. Voltage and current transducers, signal-conditioning circuitry, analog-to-digital converters (ADCs), and onboard memory enable measurement and storage of line-to-line or line-to-neutral voltage and line-current waveforms. NILMs measure all load current of the monitored electrical service. In some scenarios, such as low-voltage distribution networks, line-currents climb to hundreds of amps. Current transducers and signal conditioning circuitry process the line-current waveforms into the full-scale range of the ADC. Although there are many frequency components in the line currents, the utility-frequency component dominates and the dynamic range is insufficient for high-fidelity acquisition of the smaller-magnitude higher-frequency current signals. Most NILMs target the utility-frequency component and lower-order harmonics (such as the third, fifth, and seventh) and the signal conditioning circuitry is simply an anti-aliasing filter and scaling-and-shifting circuitry to interface with the ADC. NILMs with enhanced nonintrusive MCSA capabilities include additional conditioning and acquisition. Appropriately-designed high-pass or notch filters eliminate the utility-frequency component of the signal [10], [14], [18]. Elimination of the utility frequency and subsequent amplification of the filtered signal improves dynamic range. An additional acquisition channel samples the filtered signal.

O'Connell et al. [18] and Lee et al. [15] present the design and deployment of custom power monitor acquisition instrumentation with an adaptive notch filter for automatic utility frequency rejection. Fig. 5 shows a block diagram of the acquisition hardware. The ADCs sample up to eight

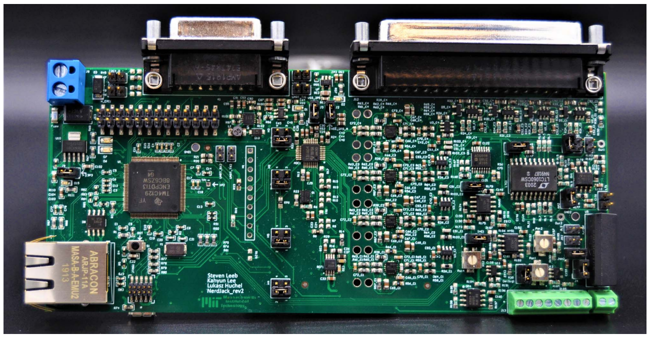

Fig. 6. Custom power monitor acquisition hardware.

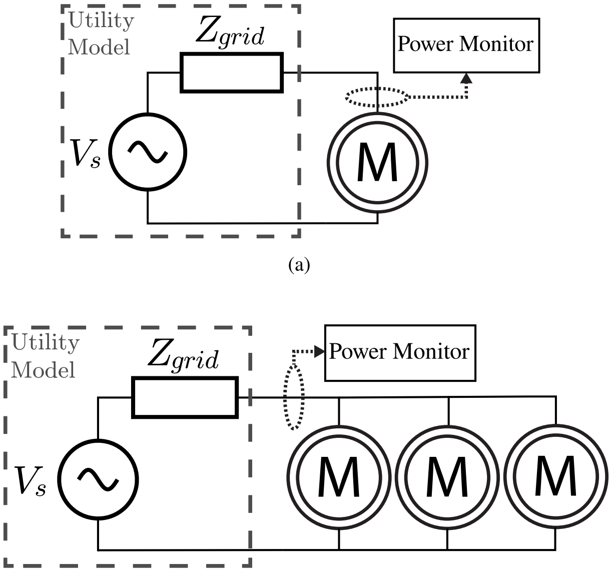

(a)

(b)

Fig. 7. Test cases (a) traditional MCSA and (b) nonintrusive MCSA.

signals. These typically include the three-phase utility voltage and current signals. If selected, one other channel samples the output of the onboard switched-capacitor notch filter. The input to the notch filter is usually a power-system current signal for current signature analysis. The device detects the zero-crossings of the selected signal and clocks a fourth-order switched capacitor (SC) notch filter integrated circuit to attenuate the utility-frequency component of the signal. It is important to note that, because of the finite Q factor, the notch filter also attenuates diagnostic current signals very close to the utility component, such as the "twice slip frequency (2sf) sidebands" indicative of cage winding defects, e.g., rotor bar damage [10]. However, with the presented hardware, the unfiltered line currents are still available for MCSA. There are dynamic-range concerns and data windowing (with inherent spectral leakage and reduced spectral resolution) limits direct spectral-analysis techniques based on the DFT, but, in some situations, parametric and other spectral-analysis techniques could extract cage winding insights from the unfiltered current [20], [26], [27], [28]. Fortunately, even if the 2sf sidebands are lost, other current signals from SCIMs in the passband of the notch filter also indicate cage-winding defects [11], [15]. Fig. 6 is a picture of the acquisition hardware. Experiments described in Sections IV and VII use this hardware for the validation of the modeling demonstrated in this work.

IV. EXAMPLE MULTIPLE-MACHINE MONITORING SCENARIO

Before the analysis focuses on the interaction between the PSH of a single SCIM and the power system, this section compares spectra from traditional MCSA and nonintrusive MCSA. The results exhibit the ability of an aggregate power monitor to measure the current signals from multiple grid-connected SCIMs. In this example, there are no meaningful current-division effects, and nonintrusive MCSA provides the same insights as three traditional MCSA monitors. Sections VI and VII present analysis and experiments of situations with significant current division. Additionally, in these results, the current signals of interest do not significantly overlap. Section VIII discusses overlap and other practical challenges of nonintrusive MCSA.

Fig. 7 presents two monitoring scenarios. Fig. 7(a) shows traditional MCSA where sensors measure the individual machine currents. Fig. 7(b) shows nonintrusive MCSA where sensors measure the aggregate current feeding many machines. In Fig. 7, Z_{cable} (as shown in Fig. 2) has been incorporated into Z_{grid}. For the experimental multiple-machine demonstration, three SCIMs were used: a three-phase Elektrim Motors 40MCM-3-.25-18 0.25 hp (186 W) motor [29], a fractional horsepower (520 W) single-phase SCIM that drives an axial fan [30], and a 1 hp (746 W) single-phase SCIM that drives a centrifugal fan [31]. Other than the power rating, detailed information on the single-phase SCIMs was not available. In general, (1) requires knowledge of SCIM parameters and load. In this experiment, the traditional MCSA measurements provide the same information as (1). The setup of Fig. 7(a) isolates machine harmonics and displays their frequency locations for that motor operating point. Operating points were held constant across tests. In each test setup, the power monitor of Section III sampled the currents at 8 kHz for 6 s and the notch filter processed the *phase a* current. Before computing the spectrum, a Blackman window function processed the measurements. The Blackman window provided an adequate trade-off between main-lobe width and side-lobe height.

The presented spectra focus on a frequency range around the PSH of the 0.25 hp motor (about 560 Hz). Any frequency range with current signals from each machine is illustrative, and the region around the PSH of the 0.25 hp motor was chosen because PSH tracking is often of interest [15], [18]. Also, for clearer visualization and spectral-leakage mitigation, a digital second-order infinite impulse response (IIR) notch filter attenuated the ninth harmonic of the motor current. The MATLAB functions *iirnotch()* and *filter()* designed the filter and filtered the signal, respectively. The IIR notch filter had a -3 dB stopband bandwidth of 6 Hz centered at nine times the detected utility frequency. For traditional MCSA, in three separate tests, the power monitor measured the individual

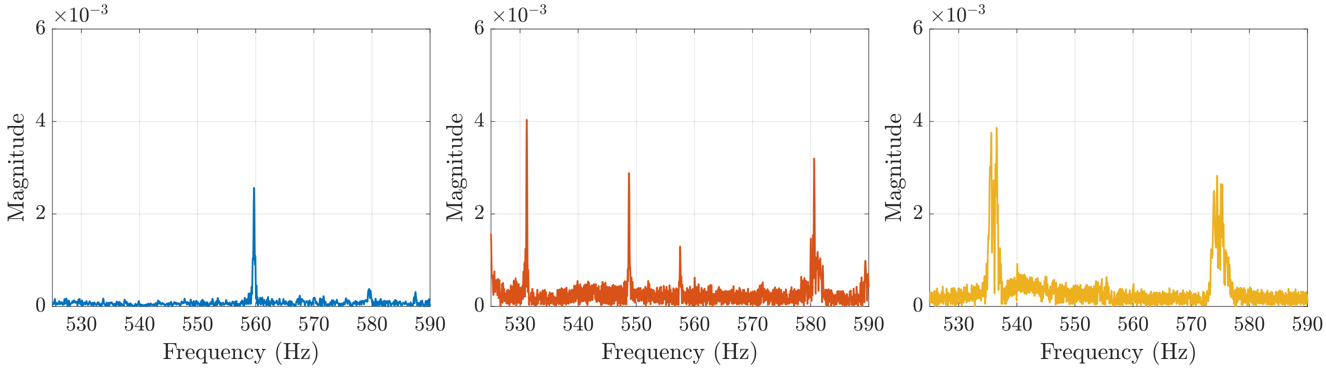

(a) (b) (c)

Fig. 8. Spectra from traditional MCSA (a) 0.25 hp motor, (b) axial-fan motor, and (c) centrifugal-fan motor.

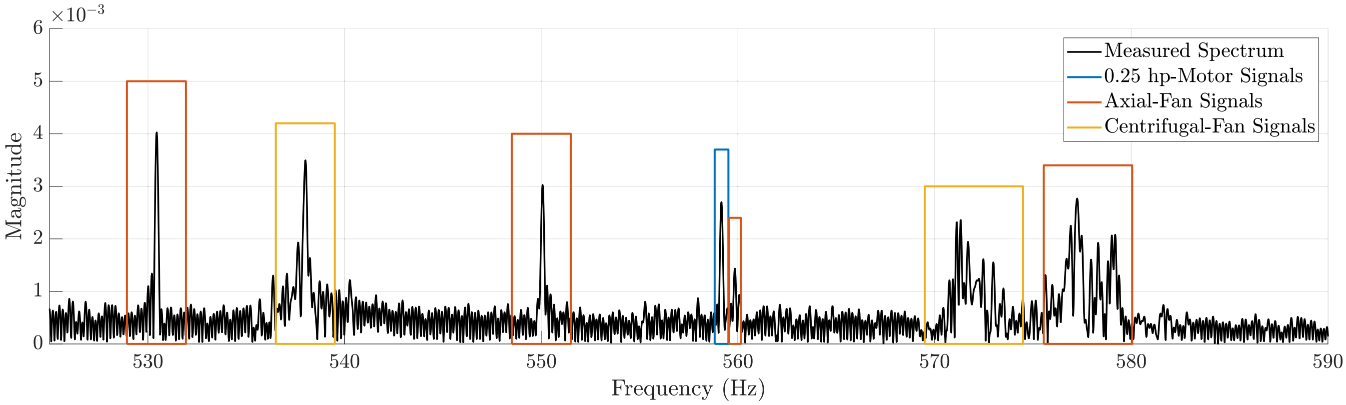

Fig. 9. Spectrum from nonintrusive MCSA. Boxes around the peaks indicate which SCIM generated the signal.

machine currents, i.e., the setup of Fig. 7(a). The single-phase machines were connected between *phase a* and the neutral of the monitored grid. Fig. 8(a) shows the *phase a* motor-current spectrum of the 0.25 hp motor from traditional MCSA. The motor was operating at an approximately rated slip of 7.8%. The PSH is located at 559.7 Hz and agrees with the frequency predicted by (2). Fig. 8(b) the shows motor-current spectrum of the axial-fan single-phase SCIM from traditional MCSA. A slot harmonic is visible around 580.6 Hz. The variation of rotor rotational speed smears the slip-dependent slot harmonic across frequency. Narrow-band 8.8 Hz sidebands around the 539.92 Hz ninth utility frequency harmonic, which itself is not visible due to the digital IIR notch filter, are located at 531.2, 548.8, and 557.5 Hz. Fig. 8(c) shows the motor-current spectrum of the centrifugal-fan single-phase SCIM from traditional MCSA. Slot harmonics are visible around 536.1 and 574.5 Hz. Like the axial fan, variation of rotor rotational speed smears the centrifugal fan slot harmonics across frequency.

Fig. 9 shows the spectrum from nonintrusive MCSA, i.e., the setup of Fig. 7(b). The power monitor measured the aggregate current feeding the three SCIMs. The aggregate-current spectrum contains the same current signals visible in the traditional MCSA. Boxes highlight each signal set. The 0.25 hp motor PSH is located at 559.1 Hz. The axial fan slot harmonic is smeared around 577 Hz. For this test, the utility frequency was about 60.02 Hz and the ninth harmonic was located at about 540.2 Hz. The sidebands have about 9.8 Hz spacing and are located at about 530.4, 550.0, and 559.8 Hz. The centrifugal-fan slot harmonics are smeared around 538 and 571 Hz.

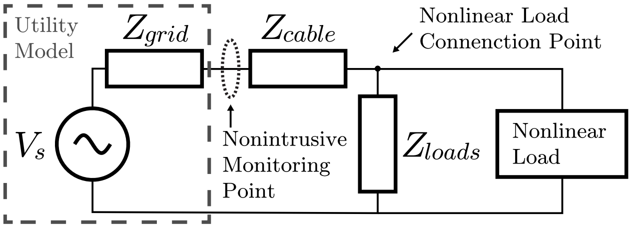

Fig. 10. Nonlinear load in a power system.

V. NONLINEAR LOADS IN POWER SYSTEMS

This section considers nonlinear loads in power systems. Section V-A reviews the current-source model for nonlinear loads. Section V-B considers a current-source model for grid-connected SCIMs.

A. Nonlinear Loads

Nonlinear loads introduce new frequency content into the voltages and currents of a power system [32]. Fig. 10 presents a circuit diagram of a nonlinear load connected to a power system. This schematic is similar to those of Fig. 2 but focuses

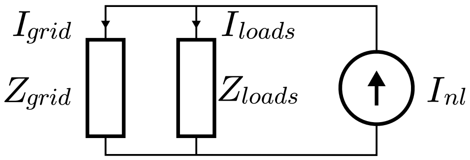

Fig. 11. Nonlinear-load equivalent circuit with current division.

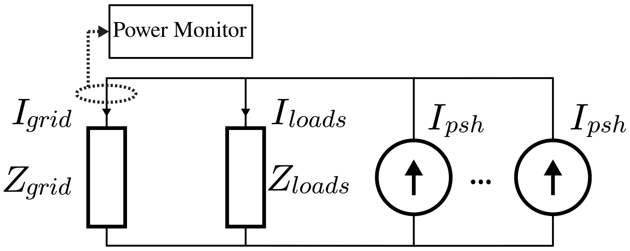

Fig. 12. Nonlinear-load equivalent circuit of a nonintrusive MCSA setup with multiple motors.

on the connection point of a specific nonlinear load. In a practical scenario, the system powers many nonlinear loads. The impedance Z_{loads} is a lumped model for all other loads and their cabling as seen from the nonlinear load connection point. For nonfundamental frequency behavior, a common model for a nonlinear load is an ideal current source that supplies currents at one or multiple frequencies with magnitudes that can depend on other circuit parameters [32], [33]. The fundamental frequency circuit is considered separately from the nonlinear load current-source circuit. Fig. 11 presents the nonlinear-load current-source circuit (with Z_{cable} included with Z_{grid}), considered at some frequency that is not present in V_s. I_{nl} is the current-source model of the nonlinear load. Written in the "s-domain" (Laplace transform), the expressions for the currents are given by the current division

$$I_{\text{loads}}(s) = \frac{Z_{\text{grid}}(s)}{Z_{\text{loads}}(s) + Z_{\text{grid}}(s)} I_{\text{nl}}(s) \tag{3}$$

$$I_{\text{grid}}(s) = \frac{Z_{\text{loads}}(s)}{Z_{\text{loads}}(s) + Z_{\text{grid}}(s)} I_{\text{nl}}(s). \tag{4}$$

The relative magnitudes of $Z_{\text{grid}}(s)$ and $Z_{\text{loads}}(s)$ dictate the propagation of current sourced by nonlinear loads. The phase of $Z_{\text{grid}}(s)$ and $Z_{\text{loads}}(s)$ will also effect the nature of the currents $I_{\text{grid}}(s)$ and $I_{\text{loads}}(s)$. Section VI further investigates the interaction between the system impedances and the current of the nonlinear load.

Equations (3) and (4) have implications for the nonintrusive MCSA of grid-connected SCIMs. As described in Section II, SCIMs are nonlinear loads. The combination of machine geometry and magnetic circuits in relative motion creates nonfundamental frequency content in the air-gap flux and induces currents at new frequencies in the stator windings. The stator windings of grid-connected SCIMs directly connect to the power system and the induced currents propagate through the branches of the power system. In general, Fig. 2(b) illustrates the impedance diagram of this scenario. Fig. 12 is the nonlinear load equivalent of Fig. 2(b) and shows multiple machines acting as PSH current sources. Fig. 12 considers nonfundamental frequencies so V_s has been replaced with a short circuit. Also, Z_{cable} has again been incorporated into Z_{grid}. The PSH frequencies are likely distinct, but there is a chance of overlap. Each SCIM produces a family of current signals, e.g., the rotor slot harmonics described by (1), and a PSH equivalent circuit is just one of many nonlinear current source equivalent circuits. The NILM measures $I_{\text{grid}}(s)$. Changes in $Z_{\text{grid}}(s)$ and $Z_{\text{loads}}(s)$ may affect the magnitude of the slot harmonics and other diagnostic-rich current signals present in $I_{\text{grid}}(s)$. This article is motivated by this example.

B. Induction Machines as a Current Source

There is a negligible change in the sourced current from high-impedance voltage sources for a wide range of connected loads. Consequently, high-impedance voltage sources are well-modeled by ideal current sources. The PSH current-source model of a SCIM is argued with similar reasoning.

The coupled-circuit approach to induction-machine spatial harmonics treats adjacent rotor bars and end caps segments as one-turn windings called rotor loops [34]. Assuming a magnetically-linear system, the voltage equations of an induction machine with any number of stator windings and rotor bars can be written in terms of the resistances and self and mutual inductances of the stator windings and rotor loops [34]. Yepes et al. [25] use the coupled circuit approach to define a PSH equivalent circuit which consists of a voltage source at the PSH frequency and associated impedances. The voltage source magnitude depends on the magnitude of the fundamental-frequency motor current and the impedances depend upon the system inductance matrices [25]. Complete knowledge of the inductance matrices is not realistic in practice.

Although not directly applicable empirically, the coupled-circuit approach aids in modeling and supports the PSH current-source model. The parallel combination of Z_{grid} and Z_{loads} is likely significantly smaller than the PSH equivalent circuit impedance and the current-source model will apply. Further, power systems are designed to keep Z_{grid} as low as possible for stability and voltage requirements. Experimental results in Section VII validate the slip-dependent PSH current-source model for a grid-connected SCIM.

VI. POWER SYSTEM MODELING

Section IV presented results where nonintrusive MCSA is effectively equivalent to traditional MCSA and demonstrated potential for nonintrusive monitoring of multiple grid-connected SCIMs. This section investigates the effect of connected loads and source impedance on the current signals measured by an aggregate power monitor. Bode plots describe how power system impedances affect the propagation of current signals from grid-connected SCIMs. The analysis focuses on the PSH because its amplitude can be reliably measured experimentally (see Section VII), however, the approach applies generally to any current signal of an SCIM, diagnostic-related or otherwise. An analysis of three scenarios with constant source impedance is presented. The three scenarios include resistive, inductive, and capacitive loads. Resistive, inductive, and capacitive loads are common in power systems. Heaters are resistive loads. Grid-connected motors are mostly inductive loads. Capacitors of electromagnetic interference (EMI) filters and power factor correction capacitor banks are capacitive loads [35]. Combinations of these elements form loads in power systems. For example, singly-tuned passive harmonic filters are a series combination of an inductor and capacitor [32]. Then, an analysis of one scenario with constant load impedance and varied source impedance is presented. The magnitude and phase of the transfer function between $I_{\mathrm{nl}}(s)$ and $I_{\mathrm{grid}}(s)$ are plotted for each scenario. A frequency range of 0–3000 Hz is considered as PSHs in this range have been documented in industrial settings [10].

A. Transfer Function H(s)

Fig. 11 describes nonintrusive MCSA, e.g., Fig. 12 for one of the machines, when

$$I_{\mathrm{nl}} = I_{\mathrm{psh}} \cos\left(2\pi f_{\mathrm{psh}} t\right) \tag{5}$$

where I_{psh} is the PSH magnitude in amperes and f_{psh} is the PSH frequency given in (2). The value of I_{psh} depends on the utility-frequency motor current amplitude and machine geometry. From (4), the transfer function $H(s)$ is defined as

$$H(s) = \frac{I_{\mathrm{grid}}(s)}{I_{\mathrm{nl}}(s)} = \frac{Z_{\mathrm{loads}}(s)}{Z_{\mathrm{loads}}(s) + Z_{\mathrm{grid}}(s)}. \tag{6}$$

This transfer function provides insight into the nature of I_{grid} measured by the aggregate power monitor and is visualized with Bode plots. Traditionally, Bode plots present the magnitude in decibels (logarithmic y-axis) and, for both magnitude and phase, use a logarithmic scale for the frequency axis. The Bode plots in this section use linear axes. In the author's opinion, in this situation, linear axes provide the most intuition due to the interpretation of magnitude as a multiplicative factor and the limited frequency range of interest.

B. Simple Loads

For these examples, Z_{grid} is represented with an R–L model with a 1 Ω resistor and an 0.95 mH inductor. These values are held constant for the first three scenarios presented in this section. The influence of different values of source impedance is investigated later in this section.

Fig. 13 presents Bode plots of the transfer function $H(s)$ for a set of resistive Z_{loads}. The resistance varies from 10 to 50 Ω in 10 Ω increments. The magnitude of the transfer function decreases for lower values of resistance. Said another way, there is higher attenuation of the PSH measured by the aggregate power monitor for lower values of Z_{load}. For all values of Z_{load}, the magnitude of the transfer function decreases monotonically with frequency because the impedance of the source branch increases linearly with frequency (inductive) and the impedance of Z_{load} is independent of frequency (resistive).

Fig. 14 presents Bode plots of the transfer function $H(s)$ for a set inductive Z_{loads}. The inductance varies from 1.5 to 3 mH in 0.5 mH increments. The magnitude of the transfer function decreases for lower values of inductance. Compared to the resistive case, different behavior is exhibited for inductive Z_{loads}. At low frequencies, for all values of inductance, the magnitude of $H(s)$ is very small and the resistive term of Z_{grid} dominates. At higher frequencies, the magnitude of $H(s)$ is nearly constant as both Z_{grid} and Z_{loads} increase linearly with frequency.

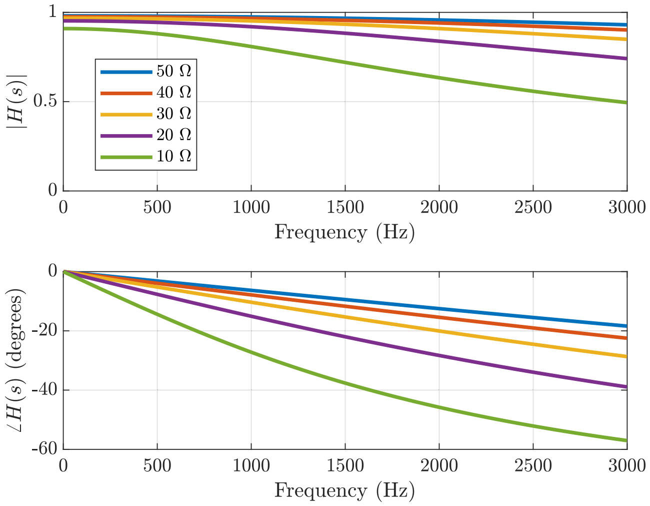

Fig. 13. Bode plots of $H(s)$ for a set of resistive Z_{loads}.

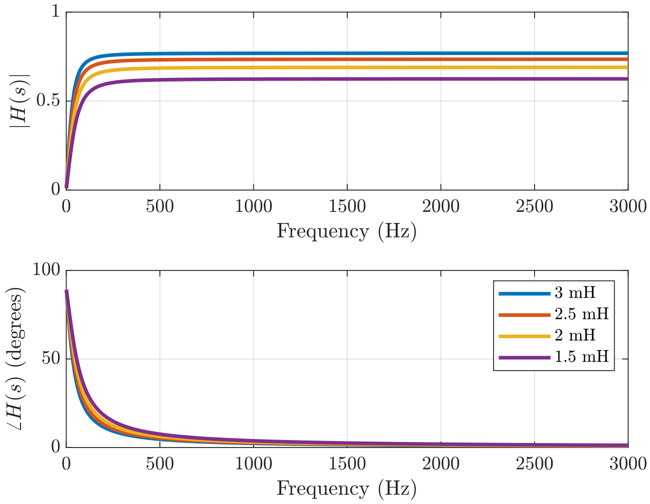

Fig. 14. Bode plots of $H(s)$ for a set of inductive Z_{loads}.

Fig. 15 presents Bode plots of the transfer function, $H(s)$ for a set of capacitive Z_{loads}. The capacitance varies from 5 to 20 μF in 5 μF increments. In this scenario, the source inductance and load capacitance resonate. The resonant frequency decreases for increased values of capacitance. Before resonance, the magnitude of $H(s)$ is greater than or equal to one. After resonance, the magnitude of $H(s)$ rolls off toward zero. Specifically, a higher proportion of the current flows through the load branch because the source inductance presents a high-impedance path and the load capacitance presents a low-impedance path.

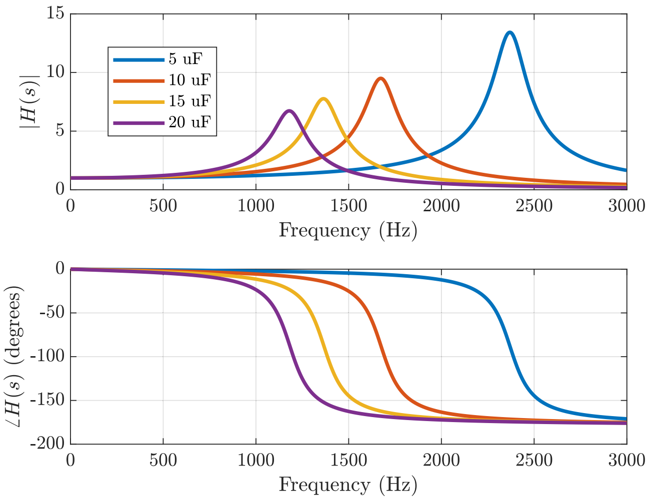

Fig. 15. Bode plots of $H(s)$ for a set of capacitive Z_{loads}.

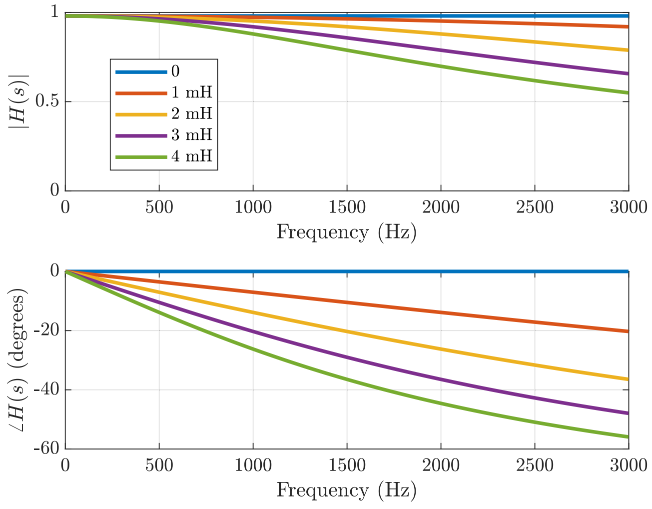

Fig. 16. Bode plots of $H(s)$ for resistive load with varying source inductance.

C. Varied Source Impedance

The previous examples illustrated the effect of different load impedances, i.e., changes in Z_{load}, on $H(s)$. For lower load impedances, a larger proportion of current flows through the load branch, which is reflected in the smaller magnitude of $H(s)$. Next, the effects of different source impedance parameters are investigated.

Fig. 16 presents Bode plots of the transfer function, $H(s)$ for a resistive Z_{loads} equal to 50 Ω and a set of source inductances. The source inductance varies from 0 to 4 mH in 1 mH increments. The magnitude plot decreases with increased source inductance. High source impedance and low load impedance have similar effects on the transfer function $H(s)$. Grids with high source impedance, i.e., weak grids, and loads that present low impedance at the PSH frequency can limit the measurement capabilities of a NILM.

VII. EXPERIMENTAL RESULTS

In this section, the modeling described in Section VI is verified experimentally. The first experiment investigates the PSH magnitude for changes in slip and source impedance. The second experiment demonstrates the attenuation of the PSH measured by a NILM due to a connected load. Experiments use the PSH for repeatable SCIM "signal-source" behavior and higher signal-to-noise ratio (SNR). As briefly mentioned in Section VI-A and verified in Section VII-B, stator currents (air-gap fluxes) at the utility frequency and its harmonics influence the magnitudes of the rotor slot harmonics. The applied stator voltages drive the stator currents. The harmonic content of the utility and laboratory three-phase power source voltage varies with time and loading, however, the magnitude of the fundamental frequency component is tightly regulated and much more consistent. Thus, the experiments use the PSH as it depends on the fundamental frequency component and not other harmonics. Additionally, as seen in Fig. 1, the PSH is often the dominant component with higher SNR compared with the other rotor slot harmonics.

TABLE I

MOTOR INFORMATION

Manufacturer	Elektrim Motors	Worldwide Electric Corporation
Model	40MCM-3-.25-18	WWEI 5-36-143JM
Poles	4	2
Power (hp)	0.25	1.5
Rated Speed (rpm)	1660	3480
Full Load Efficiency (%)	64	82.5
Rotor Bars	18	16

A. Experimental Setup

Two three-phase power sources were used for the experiments, the HP6834B ac power source/analyzer and the utility service (wall output) available in the laboratory. Each provided 208/120 V 60 Hz output. Two SCIMs were used, the Elektrim Motors 40MCM-3-.25-18 0.25 hp motor [29] coupled to the Magtrol HD-700-8 dynomometer [36] and the Worldwide Electric Corporation WWEI 5-36-143JM 1.5 hp motor [16] coupled to the Magtrol HD-810-8N dynomometer [36]. Table I contains additional motor parameters. The power monitor instrumentation of Section III was used with a personal computer for data capture and visualization [37], [38]. For all experiments, the *phase a* current was processed by the notch-filter circuitry. The notch-filter signal path has gain-setting potentiometers for the different magnitudes of nonfundamental frequency current that may be encountered across power systems. The potentiometers are set upon installation to achieve appropriate use of the ADC full-scale range during normal levels of nonfundamental frequency current and avoid saturation during periods of exceptionally high levels. Consequently, the exact scaling of the current through the acquisition path is dependent on the potentiometer settings. The current magnitudes presented in this section are scaled versions of the actual current magnitudes. The potentiometer settings were the same for all experiments and conclusions are drawn from relative changes in PSH magnitude across measurements.

The HP6834B AC source formed an independent power distribution system and the test loads were the only loads

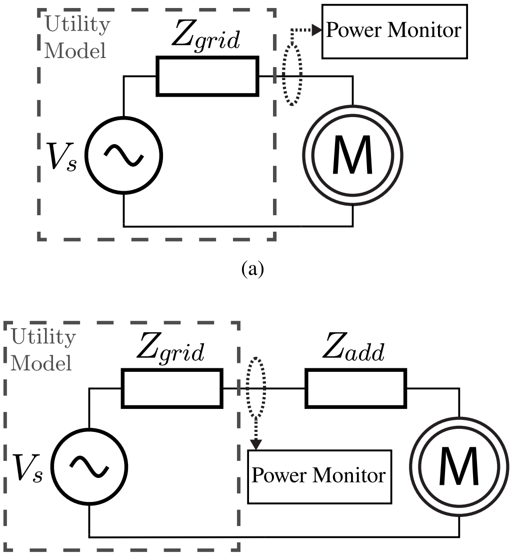

(a)

(b)

Fig. 17. Test cases (a) Scenario 1: no additional impedance and (b) Scenario 2: with additional impedance.

connected to the entire system. Tests with the utility service were similar to a situation where a power monitor is installed on a subpanel of an electrical service. That is, there are other loads connected upstream of the monitoring point. The test loads were still the only loads connected to the monitored section of the power system. In this situation, Z_{grid} encompasses generation, distribution, and other load impedances. From the characterization of the laboratory network for power-line communication and line-impedance estimation research [39], [40], [41], an RL utility model dominated by distribution and generation described the grid impedance. The agreement of predicted and estimated results in Section VII-C verifies this assumption.

B. PSH Magnitude, Slip, and Source Impedance

This experiment explores the magnitude of the PSH of a SCIM for changes in slip and source impedance. Fig. 17 presents the two test scenarios for each motor. For both scenarios, the SCIM was the only load plugged into the monitored power system and all PSH current flowed through the source branch. For Scenario 1, the source impedance consisted of the inherent source impedance of the power source and cabling. In Scenario 2, additional 0.9 mH inductors with 0.25 Ω equivalent series resistance were added to each phase to increase the source impedance. The inductors were constructed with copper wire wrapped around a MS-250026-2 toroidal powder core by Micrometals.

Fig. 18 shows the results from Scenarios 1 and 2 with the AC power source and 0.25 hp motor. This SCIM has four poles and 18 rotor bars. For the presented values of slip from lowest to highest, the corresponding PSH frequencies were very nearly the frequencies predicted by (2) of 595, 586, 573, and 558 Hz. Fig. 19 shows the results from Scenarios 1 and 2 with the utility and 1.5 hp motor. This SCIM has

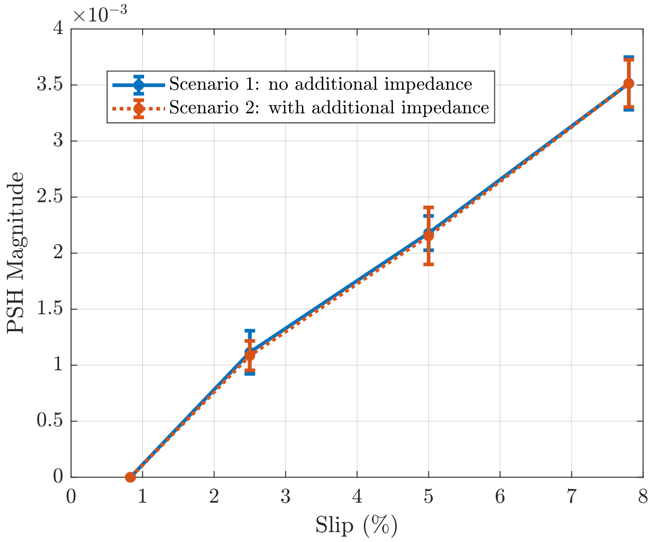

Fig. 18. PSH magnitudes of the 0.25 hp motor for Scenarios 1 and 2.

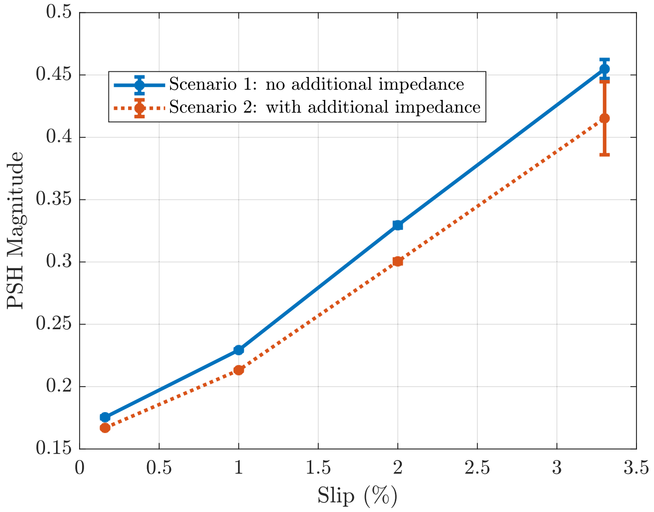

Fig. 19. PSH magnitudes of the 1.5 hp motor for Scenarios 1 and 2.

two poles and 16 rotor bars. For the presented values of slip from lowest to highest, the corresponding PSH frequencies were again very nearly the frequencies predicted by (2) of 1018, 1010, 1001, and 988 Hz. In both Figs. 18 and 19, the data points represent the average PSH magnitude from a 42 s measurement file. The measurement was partitioned into seven consecutive 6 s windows and a Blackman window function processed partition. The single-sided DFT magnitude spectrum was computed and the relative peak of the DFT within a range of 4 Hz around the expected PSH frequency location given by (2) estimated the PSH magnitude. The bounds are two standard deviations above and below the average PSH magnitude.

The PSH magnitude increases monotonically with slip. In the typical operation region for a healthy SCIM, increased slip corresponds to an increased load torque on the motor. Higher load torque demands higher motor currents and air-gap flux which induces larger PSHs. For the 0.25 hp motor, there

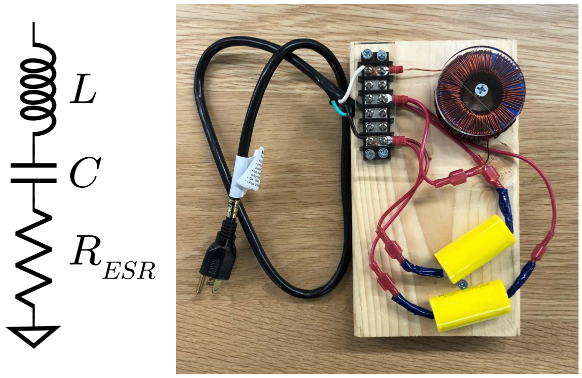

(a) (b)

Fig. 20. Passive filter (a) schematic and (b) realized filter.

is little difference between PSH magnitudes across scenarios. For the range of impedances bounded by the inherent source impedance, Z_{grid}, and the series combination of the source impedance and additional impedance, $Z_{\mathrm{grid}} + Z_{\mathrm{add}}$, this motor is well modeled by a PSH current source. For the 1.5 hp motor, the PSH magnitudes for Scenario 1 are uniformly larger than the PSH magnitudes for Scenario 2. For the range of impedances, this motor is not as well modeled as a current source. This is perhaps due to machine specific inductances and the higher PSH frequency.

Although further refinements are possible, the model of a SCIM as an ideal current source with slip-dependent magnitude has the benefits of simplicity and is very accurate in some scenarios. For most cases, loading effects from changes in Z_{grid} and Z_{loads} will be less significant compared to the current division effects. Section VII-C further demonstrates the merits of the current-source model.

C. Passive Filter

Passive singly-tuned harmonic filters are commonly deployed in power systems to attenuate the propagation of a specific current harmonic [32], [33]. The filters are a series combination of an inductor and capacitor and exhibit a notch in impedance magnitude at the resonant frequency of the inductor–capacitor system. Typically, these filters are placed close to a high-power power electronic device that is known to draw significant harmonic currents. Due to their frequent use and relatively wide notch, passive filters are candidate loads that can shunt the PSH away from a NILM. This experiment demonstrates the significant attenuation of a PSH measured by a NILM due to the connection of a passive filter to the power system. The modeling technique of Section VI predicts the PSH attenuation. A passive filter demonstrates the effect, however, attenuation of the PSH can theoretically occur with any load that presents a sufficiently low impedance at the PSH frequency.

A filter was realized and characterized. Fig. 20(a) shows the schematic of a passive singly-tuned harmonic filter. The impedance of the filter for sinusoidal steady state, $s = j\omega$, is

$$Z_{\mathrm{filter}}(j\omega) = j\left(\omega L - \frac{1}{\omega C}\right) + R_{\mathrm{ESR}}. \tag{7}$$

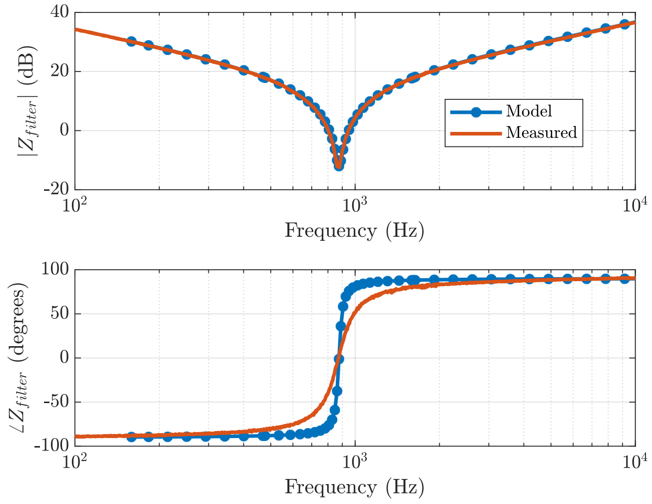

Fig. 21. Comparison of filter model and realized filter characterization.

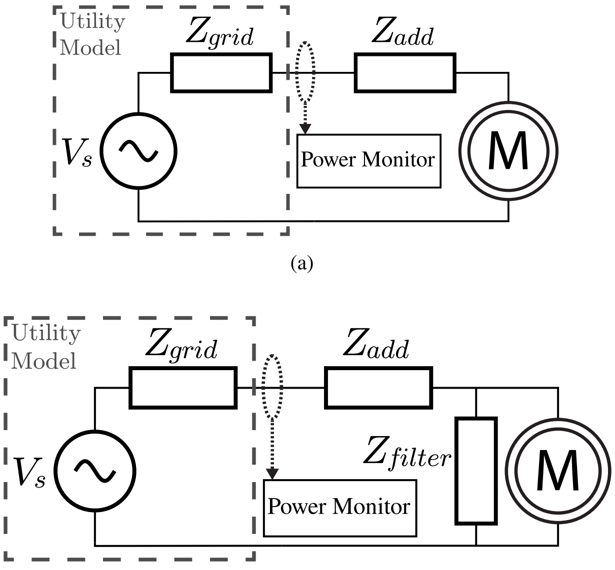

(a)

(b)

Fig. 22. Test cases (a) Scenario 1: no filter and (b) Scenario 2: filter connected.

For $\omega = 1/(LC)^{1/2}$, the impedance of the filter is equal to the combined equivalent series resistances of the inductor and capacitor, R_{ESR}. Fig. 20(b) shows the realized filter. The filter consists of a 1.1 mH inductor with 0.25 Ω equivalent series resistance and a 30 μF capacitor. Fig. 21 compares the impedance of the circuit model, i.e., (7), computed in MATLAB and experimental characterization of the realized circuit.

Fig. 22 shows the two power system scenarios. Note that each scenario included the additional source impedance. In Scenario 1, the SCIM was the only load plugged into the monitored power system. All PSH current flowed through the source branch and was measured by the power monitor. In Scenario 2, the filter was connected across *phase a* and neutral. With the filter connected, the PSH current is divided

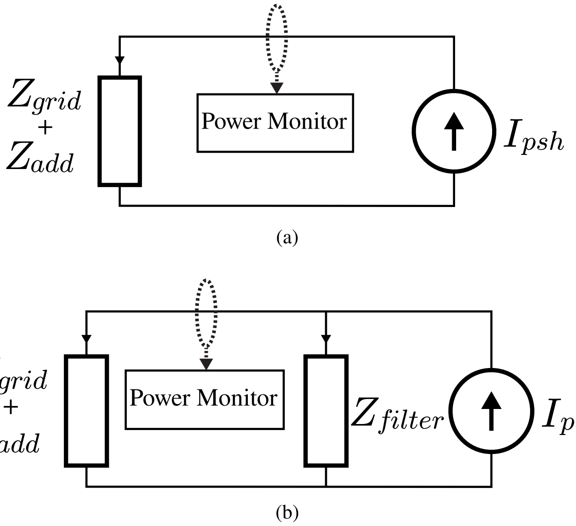

Fig. 23. PSH equivalent circuits (a) Scenario 1: no filter and (b) Scenario 2: filter connected.

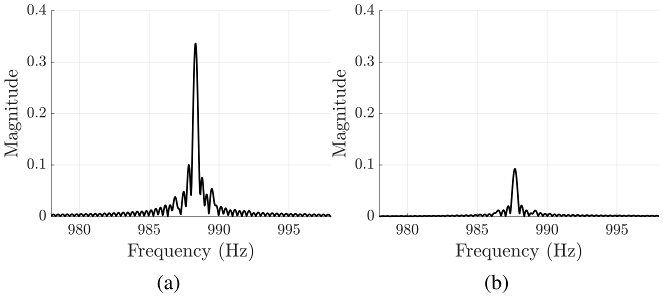

Fig. 24. PSH signal (a) Scenario 1: no filter and (b) Scenario 2: filter connected.

between the source branch and the filter-branch. Fig. 23 shows the PSH equivalent circuits for the two scenarios.

For each scenario, the notch filter output was measured for 42 s while the SCIM operated in a steady state. Fig. 24(a) and (b) present the 1.5 hp motor PSH region of the single-sided DFT magnitude spectra for Scenarios 1 and 2, respectively. For these measurements, the 1.5 hp motor shaft rotational frequency was 3528 r/min (2% slip). The filter significantly attenuates the PSH when connected to the power system.

To model the attenuation of the PSH due to the passive filter, $H(s)$ was calculated with a Z_{grid} estimate of a 1.19 Ω resistor and 52.2 μH inductor, Z_{add} equal to a 0.9 mH inductor with a 0.25 Ω equivalent series resistance, and Z_{loads} equal to the filter impedance. For this experiment, the utility was used as the ac power source. The Z_{grid} estimate was taken from [41] as the experiments presented by Saathoff et al. [41] were conducted with the same laboratory utility used in this experiment. The added source impedance emulated weak grid conditions, i.e., a low short-circuit ratio, a characteristic of many microgrids [42], [43]. The solid line in Fig. 25 shows the magnitude plot of $H(s)$. As expected, the magnitude drops significantly at the notch frequency of the filter. The data points marked with an "x" are the measured values of $H(s)$ computed by division of the average PSH magnitude with the filter connected and without the filter. The average PSH magnitudes were computed as described in Section VII-B. The data points at 558, 572, and 586 Hz are from the PSHs of the 0.25 hp motor at 7.8% (rated), 5%, and 2.5% slip, respectively. The data points at 988, 1001, and 1010 Hz are from the PSHs of the 1.5 hp motor at 3.3%, 2%, and 1% slip, respectively. The predicted $H(s)$ and the measured values of $H(s)$ agree. Possible sources of error include the Z_{grid} estimate, component tolerances, and the limitations of the current source model for the 1.5 hp motor.

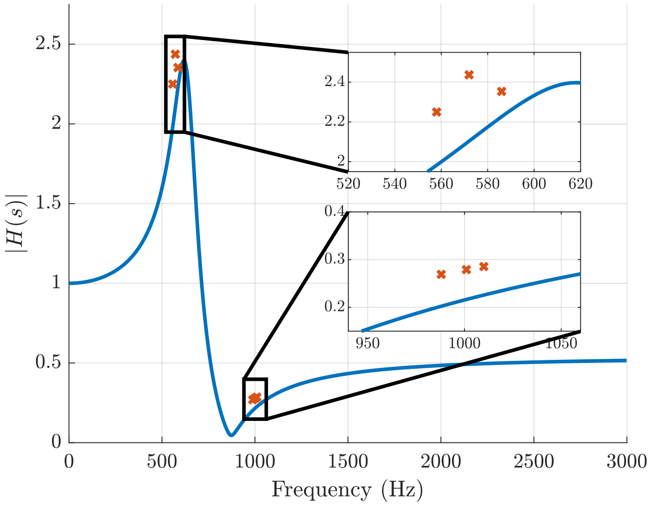

Fig. 25. Predicted $H(s)$ and measured $H(s)$ values for Z_{loads} equal to the filter.

VIII. PRACTICAL CHALLENGES AND USE CASES

The modeling and experimental verification presented in this article serve as a guide for system designers. Section VI provides designers with a way to estimate the ability of a NILM to measure current signals and provide diagnostic insights. However, several practical challenges accompany nonintrusive MCSA. The time-varying nature of power systems complicate implementation. Grid impedance, i.e., Z_{grid}, may change with temperature and load. To address this, a NILM could adjust grid-impedance estimates as the monitored currents increase. Load classification and detection provided by a NILM could also provide estimates for Z_{loads}. With knowledge of the connected loads, NILMs can adjust their conclusions "on the fly" as troublesome loads, that is loads that present low impedance at the frequencies of interest, come online. However, in practice, all loads may not be classified or accurately described by lumped linear models. Finally, current signals from different devices may interfere and overlap. Techniques from spectral analysis and signal detection theory could provide solutions, but in some cases, such as multiple machines of the same model, overlap may impede analysis. O'Connell et al. [15] present a slot harmonic disaggregation technique for nonintrusive MCSA.

IX. CONCLUSION

This article demonstrated the implications of current division for nonintrusive MCSA. A modeling technique predicted the attenuation of PSH current signals measured by an aggregate power monitor. Experimental results confirmed the modeling technique. The presented methods enable a facilities manager, or grid or equipment operator to concisely determine the conditions under which an aggregate power monitor can perform the work of several traditional individual MCSA monitors.

REFERENCES

[1] M. Lopez-Ramirez, C. Rodriguez-Donate, L. M. Ledesma-Carrillo, F. J. Villalobos-Pina, J. U. Munoz-Minjares, and E. Cabal-Yepez, "Walsh–Hadamard domain-based intelligent online fault diagnosis of broken rotor bars in induction motors," *IEEE Trans. Instrum. Meas.*, vol. 71, pp. 1–11, 2022.

[2] H. Li, G. Feng, D. Zhen, F. Gu, and A. D. Ball, "A normalized frequency-domain energy operator for broken rotor bar fault diagnosis," *IEEE Trans. Instrum. Meas.*, vol. 70, pp. 1–10, 2021.

[3] R. Puche-Panadero, J. Martinez-Roman, A. Sapena-Bano, and J. Burriel-Valencia, "Diagnosis of rotor asymmetries faults in induction machines using the rectified stator current," *IEEE Trans. Energy Convers.*, vol. 35, no. 1, pp. 213–221, Mar. 2020.

[4] D. T. Hoang and H. J. Kang, "A motor current signal-based bearing fault diagnosis using deep learning and information fusion," *IEEE Trans. Instrum. Meas.*, vol. 69, no. 6, pp. 3325–3333, Jun. 2020.

[5] J. Li, Y. Wang, Y. Zi, X. Sun, and Y. Yang, "A current signal-based adaptive semisupervised framework for bearing faults diagnosis in drivetrains," *IEEE Trans. Instrum. Meas.*, vol. 70, pp. 1–12, 2021.

[6] J. E. Garcia-Bracamonte, J. M. Ramirez-Cortes, J. de Jesus Rangel-Magdaleno, P. Gomez-Gil, H. Peregrina-Barreto, and V. Alarcon-Aquino, "An approach on MCSA-based fault detection using independent component analysis and neural networks," *IEEE Trans. Instrum. Meas.*, vol. 68, no. 5, pp. 1353–1361, May 2019.

[7] E. Elbouchikhi, V. Choqueuse, F. Auger, and M. El Hachemi Benbouzid, "Motor current signal analysis based on a matched subspace detector," *IEEE Trans. Instrum. Meas.*, vol. 66, no. 12, pp. 3260–3270, Dec. 2017.

[8] L. A. Trujillo-Guajardo, J. Rodriguez-Maldonado, M. A. Moonem, and M. A. Platas-Garza, "A multiresolution Taylor–Kalman approach for broken rotor bar detection in cage induction motors," *IEEE Trans. Instrum. Meas.*, vol. 67, no. 6, pp. 1317–1328, Jun. 2018.

[9] W. T. Thomson and M. Fenger, "Current signature analysis to detect induction motor faults," *IEEE Ind. Appl. Mag.*, vol. 7, no. 4, pp. 26–34, Jul. 2001.

[10] W. T. Thomson and I. Culbert, *Current Signature Analysis for Condition Monitoring of Cage Induction Motors: Industrial Application and Case Histories*. Hoboken, NJ, USA: Wiley, 2017.

[11] A. Khezzar, M. Y. Kaikaa, M. E. K. Oumaamar, M. Boucherma, and H. Razik, "On the use of slot harmonics as a potential indicator of rotor bar breakage in the induction machine," *IEEE Trans. Ind. Electron.*, vol. 56, no. 11, pp. 4592–4605, Nov. 2009.

[12] M. Ishida and K. Iwata, "A new slip frequncy detector of an induction motor utilizing rotor slot harmonics," *IEEE Trans. Ind. Appl.*, vol. IA-20, no. 3, pp. 575–582, May 1984.

[13] K. D. Hurst and T. G. Habetler, "Sensorless speed measurement using current harmonic spectral estimation in induction machine drives," *IEEE Trans. Power Electron.*, vol. 11, no. 1, pp. 66–73, Jan. 1996.

[14] U. A. Orji et al., "Non-intrusive induction motor speed detection," *IET Electr. Power Appl.*, vol. 9, no. 5, pp. 388–396, Apr. 2015.

[15] J. W. O'Connell et al., "Nonintrusive ventilation system diagnostics," *IEEE Sensors J.*, vol. 21, no. 17, pp. 19268–19278, Sep. 2021.

[16] Worldwide Electric Corp. (2022). *Close Coupled Pump Motors WWE LV Motors*. [Online]. Available: https://wwemotors.com/close-coupled-pump.html#simple2

[17] S. R. Shaw, S. B. Leeb, L. K. Norford, and R. W. Cox, "Nonintrusive load monitoring and diagnostics in power systems," *IEEE Trans. Instrum. Meas.*, vol. 57, no. 7, pp. 1445–1454, Jul. 2008.

[18] K. Lee, L. Huchel, D. H. Green, and S. B. Leeb, "Automatic power frequency rejection instrumentation for nonintrusive frequency signature tracking," *IEEE Trans. Instrum. Meas.*, vol. 70, pp. 1–11, 2021.

[19] L. Norford and N. Mabey, "Non-intrusive electric load monitoring in commercial buildings," in *Proc. Symp. Improving Building Syst. Hot Humid Climates*, 1992, pp. 1–8.

[20] R. Cox and P. Parikh, "Algorithm for tracking the health of multiple induction motors using bus- level current," in *Proc. IECON 44th Annu. Conf. IEEE Ind. Electron. Soc.*, Oct. 2018, pp. 373–378.

[21] Philip L. Alger," *Induction Machines: Their Behav. Uses*. Gordon and Breach Publishers, 1970.

[22] P. C. Krause, O. Wasynczuk, S. D. Sudhoff, and S. Pekarek, *Analysis of Electric Machinery and Drive Systems*. Hoboken, NJ, USA: Wiley, 2013.

[23] S. Nandi, "Modeling of induction machines including stator and rotor slot effects," *IEEE Trans. Ind. Appl.*, vol. 40, no. 4, pp. 1058–1065, Jul. 2004.

[24] S. Nandi, S. Ahmed, and H. A. Toliyat, "Detection of rotor slot and other eccentricity related harmonics in a three phase induction motor with different rotor cages," *IEEE Trans. Energy Convers.*, vol. 16, no. 3, pp. 253–260, Sep. 2001.

[25] A. G. Yepes et al., "Selection criteria of multiphase induction machines for speed-sensorless drives based on rotor slot harmonics," *IEEE Trans. Ind. Electron.*, vol. 63, no. 8, pp. 4663–4673, Aug. 2016.

[26] A. V. Oppenheim and R. W. Schafer, *Discrete Time Signal Processing*. London, U.K.: Pearson, 2013.

[27] W. A. Gardner, *Statistical Spectral Analysis*. Upper Saddle River, NJ, USA: Prentice-Hall, 1988.

[28] S. M. Kay, *Modern Spectral Estimation*. Upper Saddle River, NJ, USA: Prentice-Hall, 1988.

[29] Elektrim Motors. (2022). *Metric IEC Motors 40MCM-3-.25-18*. [Online]. Available: https://www.elektrimmotors.com/dbmotors/40mcm-3-.25-18

[30] Vevor. *12' Industrial Fan Ventilator Fume Extractor Blower Telescopic Heavy Duty Garage*. Accessed: Aug. 17, 2022. [Online]. Available: https://www.vevor.com/portable-utility-blower-c_10374/12-industrial-fan%-ventilator-fume-extractor-blower-telescopic-heavy-duty-garage-p_010416942989

[31] MOUNTO. *Mounto 3-Speed Air Mover 1hp*. Accessed: Aug. 17, 2022. [Online]. Available: https://www.amazon.com/MOUNTO-3-Speed-Blower-Monster-Carpet/dp/B00R288L%8G

[32] J. C. Das, *Power System Harmonics and Passive Filter Designs*. Hoboken, NJ, USA: Wiley, 2015.

[33] A. A. Sallam and O. P. Malik, *Electric Distribution Systems*. Hoboken, NJ, USA: Wiley, 2019.

[34] H. Fudeh and C. Ong, "Modeling and analysis of induction machines containing space harmonics—Part I: Modeling and transformation," *IEEE Trans. Power App. Syst.*, vol. PAS-102, no. 8, pp. 2608–2615, Aug. 1983.

[35] H. W. Ott, *Electromagnetic Compatibility Engineering*. Hoboken, NJ, USA: Wiley, 2009.

[36] Magtrol. (2022). *Magrol Hd Series Hysteresis Dynamometers*. [Online]. Available: https://www.magtrol.com/wp-content/uploads/hd.pdf

[37] J. Donnal, "Joule: A real-time framework for decentralized sensor networks," *IEEE Internet Things J.*, vol. 5, no. 5, pp. 3615–3623, Oct. 2018.

[38] J. S. Donnal, "Wattsworth: An open-source platform for decentralized sensor networks," *IEEE Internet Things J.*, vol. 7, no. 1, pp. 189–196, Jan. 2020.

[39] A. O. Aderibole, E. K. Saathoff, K. J. Kircher, S. B. Leeb, and L. K. Norford, "Power line communication for low-bandwidth control and sensing," *IEEE Trans. Power Del.*, vol. 37, no. 3, pp. 2172–2181, Jun. 2022.

[40] A. O. Aderibole, K. J. Kircher, S. B. Leeb, and L. K. Norford, "Distributed load control using reliable low-data-rate power line communication," *IEEE Access*, vol. 10, pp. 50242–50253, 2022.

[41] E. K. Saathoff, S. R. Shaw, and S. B. Leeb, "Line impedance estimation," *IEEE Trans. Instrum. Meas.*, vol. 70, pp. 1–10, 2021.

[42] A. Adib, B. Mirafzal, X. Wang, and F. Blaabjerg, "On stability of voltage source inverters in weak grids," *IEEE Access*, vol. 6, pp. 4427–4439, 2018.

[43] D. Kumar and F. Zare, "A comprehensive review of maritime microgrids: System architectures, energy efficiency, power quality, and regulations," *IEEE Access*, vol. 7, pp. 67249–67277, 2019.

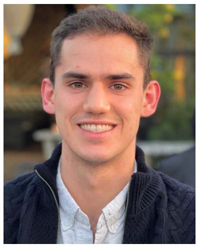

Thomas C. Krause (Graduate Student Member, IEEE) received the B.S. degree in electrical engineering from Purdue University, West Lafayette, IN, USA, in 2019, and the M.S. degree in electrical engineering and computer science from the Massachusetts Institute of Technology, Cambridge, MA, USA, in 2021, where he is currently pursuing the Ph.D. degree in electrical engineering and computer science.

Łukasz Huchel received the B.Sc. degree in electrical power engineering from the Silesian University of Technology, Gliwice, Poland, in 2013, the M.Sc. degree from the Department of Electrical Engineering and Computer Science (EECS), Masdar Institute of Science and Technology, Abu Dhabi, United Arab Emirates, in 2015, and the Ph.D. degree from the Massachusetts Institute of Technology, Cambridge, MA, USA, in 2021.

He is currently with Enphase Energy, Austin, TX, USA.

Daisy H. Green (Member, IEEE) received the B.S. degree in electrical engineering from the University of Hawai‘i at Mānoa, Honolulu, HI, USA, in 2015, and the M.S. and Ph.D. degrees in electrical engineering and computer science from the Massachusetts Institute of Technology (MIT), Cambridge, MA, USA, in 2018 and 2022, respectively.

She is currently a Post-Doctoral Associate with the Department of Architecture, MIT. Her research interests include the development of signal processing algorithms for energy management and condition monitoring.

Kahyun Lee received the B.S. and Ph.D. degrees in electrical engineering from Seoul National University, Seoul, South Korea, in 2013 and 2018, respectively.

From 2018 to 2020, she was a Post-Doctoral Associate at the Massachusetts Institute of Technology, Cambridge, MA, USA. From 2020 to 2021, she worked as a Senior Engineer at Samsung Electronics Corporation, Suwon, South Korea. Since 2021, she has been with the Department of Electronic and Electrical Engineering, Ewha Womans University, Seoul, where she is currently an Assistant Professor. Her research interests include electric machine control, condition monitoring, and energy conversion.

Steven B. Leeb (Fellow, IEEE) received the Ph.D. degree from the Massachusetts Institute of Technology (MIT), Cambridge, MA, USA, in 1993.

He has served as a Commissioned Officer for the USAF Reserves. Since 1993, he has been a member of the faculty with the Department of Electrical Engineering and Computer Science, MIT. He also holds a joint appointment with the Department of Mechanical Engineering, MIT. He is the author or coauthor of over 200 publications and 20 U.S. patents in the fields of electromechanics and power electronics.